Desalination and Water Treatment
www.deswater.com

doi: 10.5004/dwt.2022.28796

271 (2022) 272–280
September

Effective photocatalytic degradation of dye pollution in synthetic wastewater using nanocomposites of chromium and potassium oxides

D. Hamad[a], Sameh S. Ahmed[b,c], M.I. Sayyed[d], M. Rashad[a,e,*]

[a]*Physics Department, Faculty of Science, Assiut University, Assiut 71516, Egypt, email: m.rashad@aun.edu.eg (M. Rashad)*
[b]*Mining and Metallurgical Engineering Department, Faculty of Engineering, Assiut University, Assiut 71516, Egypt*
[c]*Civil and Environmental Engineering Department, College of Engineering, Majmaah University,*
Al-Majmaah 11952, Saudi Arabia
[d]*Department of Physics, Faculty of Science, Isra University, Amman, Jordan*
[e]*Physics Department and Nanotechnology Research Units, Faculty of Science, Tabuk University, Tabuk, Saudi Arabia*

ABSTRACT

In the present work, chromium(III) oxide (Cr_2O_3) and potassium oxide (K_2O) nanoparticles (NPs) were synthesized using the combustion method. Mixed oxides of varying concentrations in the form of $(1–x)Cr_2O_3/xK_2O$ (x = 0.1, 0.3, 0.5, and 0.7) were prepared. X-ray diffraction (XRD), high-resolution transmission electron microscopy (HRTEM), and optical measurements were used to investigate the properties of NPs. XRD indicates that the grain size of the mixed oxides decreased as the K_2O content increased. Additionally, HRTEM revealed several types of shapes, such as hexagonally shaped NPs. The optical measurements showed a blue shift, indicating that the band structure was slightly modified during the Cr_2O_3/xK_2O mixing. The optical band gap obeys the direct allowed transition and varies from 2.29 to 2.59 eV as the K_2O ratio in the composites increases from x = 0.1 to 0.7. The $(1–x)Cr_2O_3/xK_2O$ NPs were used as catalysts in wastewater during a photocatalytic process. Orange G was chosen as an impurity in the water. The absorbance curves of Orange G in the water were measured at different times in the presence of the same quantity of Cr_2O_3/xK_2O NPs. It was found that after 120 min, the efficiency reached 11% and 33% for $(1–x)Cr_2O_3/xK_2O$ NPs with x = 0.1 and 0.7, respectively. Furthermore, the experimental results were analyzed by pseudo-first-order model. A first-order kinetic model had the best fit for the $(1–x)Cr_2O_3/xK_2O$ NPs. The strongest relationship occurred with a composition of $0.1Cr_2O_3/0.7K_2O$. The formed composites could be used to degrade organic dyes for water purification.

Keywords: Cr_2O_3; K_2O; High-resolution transmission electron microscopy; Photocatalysis; Optical properties; Dye pollution

1. Introduction

Environmental pollution has recently emerged as one of the most serious issues in the modern world, with a large number of people dying each year and many more suffering from chronic illnesses. Drinkable water is becoming increasingly scarce as a result of contamination of source water. Water pollution is exacerbated by the extensive presence of organic contaminants, particularly dyes, in industrial effluent from the textile, garment, leather, leather goods, footwear, and paper sectors. Moreover, artificial dyes are used in nearly every area of the consumer products industry. Furthermore, industrial effluents collected after various operations are typically highly colorful, non-biodegradable, poisonous, and carcinogenic and contain harmful colored pigments. Both artificial and organic colors are resistant to sunshine and other degradative environmental factors. Before industrial effluents are discharged into the aquatic environment, they must be remedied. In particular, dyes are discharged by many dye industries and homes through wastewater into the environment. Research is currently being conducted to develop semiconductor

---

* Corresponding author.

photocatalysts that can be used to remedy this damage through water disinfection, hazardous waste remediation, and water purification [1–4].

Metal oxides are important in environmental science, electrochemistry, biology, chemical sensors, magnetics, and other fields. Chromium oxide (Cr_2O_3) is one of the most crucial transition metal oxides and is widely used in many industries as a semiconductor photocatalyst. Chromium oxide is a p-type semiconductor with wide band gap energy (~3 eV) [5], also possesses excellent optical and electrical properties, is of low cost, chemically stable, and nontoxic, and has surface properties that affect its usage as an industrial catalyst in many reactions [6–8]. Chromium has different stable oxidation states; hence, the formation and properties of chromium oxide (Cr_2O_3) are essential for applied applications, such as in high-temperature-resistant materials [9], corrosive resistant materials [10], liquid crystal displays [11–13], green pigment, and catalysts. Mixing metal oxides with specific elements is the most effective way to improve and control their electrical and optical properties [14]. However, the preparation of Cr_2O_3/K_2O catalysts has not been studied.

This study aims to prepare $(1–x)Cr_2O_3/xK_2O$ nanomaterials with different K_2O contents. Pure K_2O mixed Cr_2O_3 NPs (nanoparticles) were synthesized through combustion. The structural and optical characterizations of these NPs were characterized using X-ray diffraction (XRD), transmission electron microscopy (TEM), and UV-Vis spectroscopy techniques. Finally, applications of the synthesized nanomaterials, such as photocatalysts, were studied for the degradation of organic Gs (Orange G). Orange G is extensively used in the textile and dyeing industries. There is no available report on the electrochemical degradation of Orange G. The effect of K_2O mixed Cr_2O_3 in different concentrations, quantities, and irradiation time on the photocatalytic performance was examined.

2. Materials and methods

2.1. Dyes and materials

The structure of Orange G dye ($C_{16}H_{10}N_2Na_2O_7S_2$), a crystal orange color anionic dye (C.I.16230, m.w. 452.37 g/mol), is illustrated in Fig. 1. $Cr(NO_3)_2·6H_2O$, $K(NO_3)_2·6H_2O$, and $CO(NH_2)_2·6H_2O$ were used in the research work. All chemicals used were of an analytical grade without any additional purifications. The deionized water was used as the solvent for all experiments.

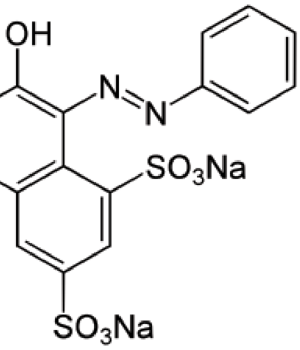

Fig. 1. Orange G chemical structure.

2.2. K_2O/Cr_2O_3 nanocomposite preparation

Combustion was used to prepare Cr_2O_3 NPs [15–17]. Then, 25 mL of a water solution containing 0.1 M $Cr(NO_3)_2·6H_2O$ was mixed with 25 mL of a water solution containing 0.1 M $Co(NH_2)_2·6H_2O$. Then the mixture was heated for 20 min in a 650 W microwave oven. Cr_2O_3 NPs of green powder was extracted. The procedure was used for preparing K_2O NPs using 0.1 M $K(NO_3)_2·6H_2O$ as a starting material. A mixture of Cr_2O_3/K_2O powder was prepared with different concentrations of $(1–x)Cr_2O_3/xK_2O$, where $x = 0.1$, 0.3, 0.5, and 0.7.

2.3. Characterizations

CuKα radiation (λ = 1.546 Å) was used in the X-ray (Philips PW 1710 X-ray Diffractometer) to study the crystal structure at temperatures between 5°C and 90°C. JCPDS-ICDD was used to analyze the XRD phases. High-resolution transmission electron microscopy (HRTEM, JEM-2100) was used to analyze the images of the prepared NPs. Additionally, scanning image observation was used for bright and dark-field TEM at 200 kV. Absorption was used for optical measurements at wavelengths from 200 to 900 nm.

The photocatalytic effect was illustrated by the Orange G degradation rate using $(1–x)Cr_2O_3/xK_2O$ NPs, where $x = 0.1$, 0.3, 0.5, and 0.7. NPs as a catalyst. Then, 2 mg of these NPs was added to 3 mL of Orange G solution. The solution was added in the ultrasonic instrument for 10 min and then transferred to glass tubes under an ultraviolet lamp with a power of 6 W separated by 15 cm. The absorbance of the solution Orange G in the presence of the catalysis $(1–x)Cr_2O_3/xK_2O$ NPs, where $x = 0.1$, 0.3, 0.5, and 0.7, was measured in a range of time of 0–120 min.

3. Results and discussion

3.1. Structural characterization

Fig. 2 depicts the XRD patterns of $(1–x)Cr_2O_3/xK_2O$ NPs, where $x = 0.1$, 0.3, 0.5, and 0.7. The XRD analysis pattern of the $(1–x)Cr_2O_3/xK_2O$ nanocomposite agrees well with standard JCPDS No. 00-026-1327 (K_2O) and 04-021-0178 (Cr_2O_3), confirming the existence of two phases in the single matrix. The observed diffraction peaks were monoclinic structures of Cr_2O_3 and hexagonal structures of K_2O. Several observations with increasing K_2O content can be illustrated with XRD charts. There is a shift in peaks (–112), (–204), (020), (–113), and (–316) to small diffraction angles, indicating the incorporation of K_2O with the Cr_2O_3 matrix. Moreover, by adding K_2O with varying concentrations, diffraction peaks related to the K_2O phase were observed at $2\theta \approx 25.08°$, 27.07°, 29.08°, 29.72°, 31.23°, and 38.76°. Lastly, the figure confirms that most of the mixture is composed of Cr_2O_3.

The size and strain of the Cr_2O_3 crystals were estimated using the Scherrer formula [18]:

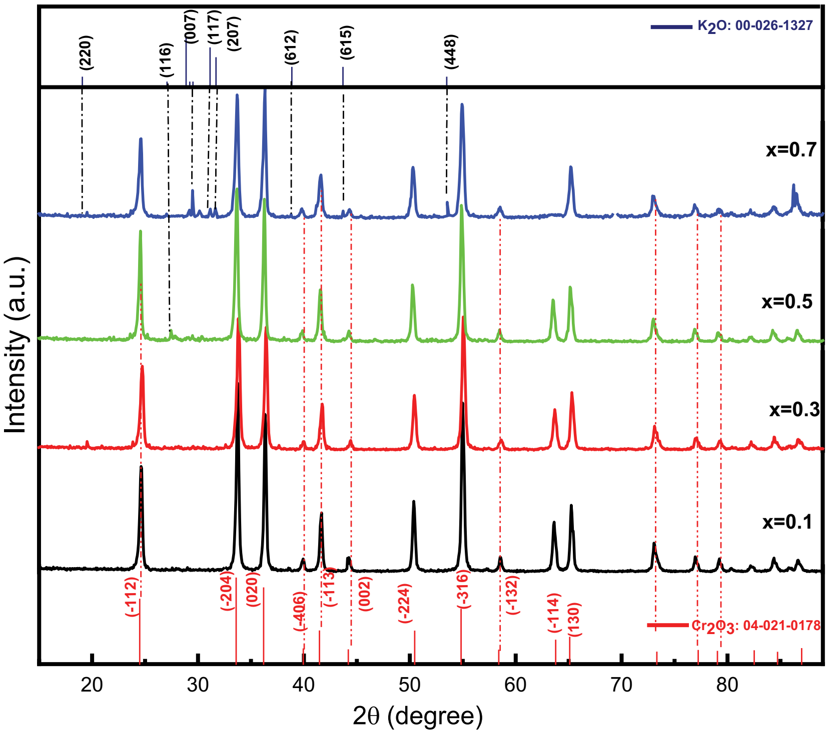

Fig. 2. XRD patterns of $(1-x)Cr_2O_3/xK_2O$ NPs. prepared in different percentages ($x = 0.1, 0.3, 0.5, 0.7$).

$$D = \frac{0.9\lambda}{\beta\cos\theta} \tag{1}$$

$$\varepsilon = \frac{\beta}{4\tan\theta}, \tag{2}$$

where D is the crystalline size, λ is the radiation wavelength, and β is the full width at half maximum at diffraction angle 2θ. Celref unit cell software was employed to calculate lattice parameters from the XRD data. The calculated lattice parameters and d-spacing of Cr_2O_3 were compared to the standard data recorded in Card No. 04-021-0178, which are listed in Table 1. This table shows that the average crystalline size decreased with increasing K_2O concentration from 33.54 to 28.37 nm.

The HRTEM images of $(1-x)Cr_2O_3/xK_2O$, where $x = 0.1$ and 0.7, are shown in Fig. 3. The TEM observations provide information about shape and size. It was found that the average diameter of $(1-x)Cr_2O_3/xK_2O$ NPs, where $x = 0.1$ and 0.7, is ~100 and 70 nm, respectively. Different shapes, such as irregularly shaped and hexagonally shaped nanoparticles, are also visible. The inset electron diffraction pattern (SAED) taken from the selected Cr_2O_3 NPs confirms the XRD pattern.

3.2. *Optical spectra of the nanoparticles*

The changes in optical absorption spectra of $(1-x)Cr_2O_3/xK_2O$, where $x = 0.1$, 0.3, 0.5, and 0.7, are shown in Fig. 4. The absorption edge of the $(1-x)Cr_2O_3/xK_2O$ samples varies with the varying content of K_2O in the Cr_2O_3 nanoparticles. As K_2O content increases, a blue shift of the optical band gap can be clearly observed, which indicates a minor modification in the band structure when mixing Cr_2O_3/xK_2O. The absorption coefficient α was calculated for each wavelength using the following equation [19]:

$$\alpha = \frac{2.3A}{t} \tag{3}$$

where A is the absorbance equal to $\log I_o/I$ (according to Beer–Lambert's law), $t = 1$ cm is the path length, and I_o and I are the intensity of incident and transmitted light, respectively.

The dependence of absorption spectra on the optical band gap energy (E_g) was described by Tauc's expression [19,20]:

$$\alpha h\upsilon = \beta\left(h\upsilon - E_g\right)^r \tag{4}$$

where β is the constant and $r = ½$ for direct transition due to photon absorption. The plot of $(\alpha h\upsilon)^2$ vs. $h\upsilon$, as shown in Fig. 5, is linear at the absorption edge, indicating a direct transition. The energy gap is determined by extrapolating the straight-line portion of the energy axis at $(\alpha h\upsilon)^2 = 0$. It is observed that the resultant values of E_g range from 2.29 to 2.59 eV as the K_2O content increases from $x = 0.1$ to $x = 0.7$ as shown in Fig. 5.

3.3. *Photocatalysis applications of Cr_2O_3/K_2O NPs*

Photocatalytic debasement is a procedure for disposing of both organic and inorganic contaminants in wastewater,

Table 1
Physical and chemical characteristics of $(1–x)Cr_2O_3/xK_2O$ nanoparticles

x	Average crystallite size (nm)	Lattice parameter [Å] (a, b, c)	Unit cell volume (Å^3)	Microstrain (ε)	Band gap (E_g)
0.1	33.54	7.2974 4.9486 5.3495	192.04	0.003415	2.34
0.3	32.88	7.2914 4.9549 5.3506	192.22	0.003443	2.24
0.5	28.81	7.3009 4.9605 5.3605	193.04	0.003972	2.44
0.7	28.37	7.2928 4.9700 5.3540	192.97	0.003996	2.59

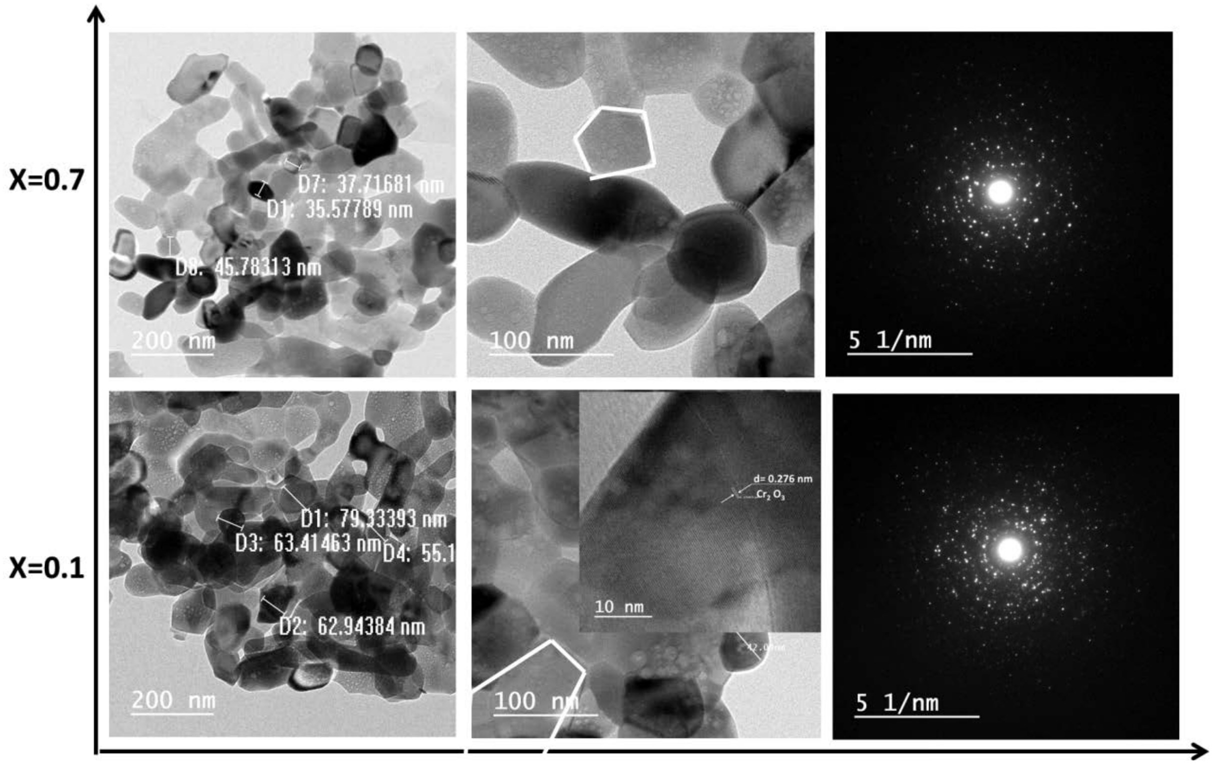

Fig. 3. Typical HRTEM images of $(1–x)Cr_2O_3/xK_2O$ where (x = 0.1 and 0.7) NPs.

where distinctive nanoparticles are utilized to eliminate these contaminants. Metal oxides are particularly effective catalysts on the other hand; mixed NPs could have an even greater efficiency. Therefore, $(1–x)Cr_2O_3/xK_2O$ NPs, where x = 0.1, 0.3, 0.5, and 0.7, were tested as catalysts with varying contents of K_2O NPs. Fig. 6 shows Orange G absorption spectra for $(1–x)Cr_2O_3/xK_2O$ NPs, where x = 0.1, 0.3, 0.5, and 0.7 at various exposure times. It can be seen that the absorbance of Orange G is distinguished by one peak at 480 nm. Moreover, these spectra show that Orange G was diminishing as the UV light time increments for each $(1–x)Cr_2O_3/xK_2O$ NP, where x = 0.1, 0.3, 0.5, and 0.7. To quantify the impact of K_2O content (x), the photocatalytic efficiency (η%) of Orange G was determined with the following equation [21,22]:

$$\eta\% = \frac{C_o - C_t}{C_o} \times 100 = \frac{A_o - A_t}{A_o} \times 100 \quad (5)$$

where C_o is the initial Orange G concentration, C_t is the residual Orange G concentration after the specified time,

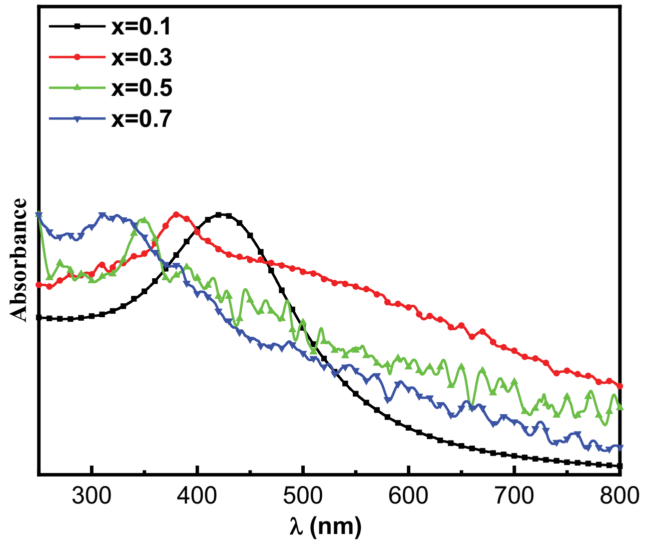

Fig. 4. UV-Vis Spectrum of (1–x)Cr_2O_3/$x$$K_2O$ (x = 0.1, 0.3, 0.5, 0.7) NPs.

A_o is the initial Orange G absorbance, and A_t is the residual Orange G absorbance after the specified irradiated time. Fig. 7 shows the photocatalytic efficiency of Orange G with (1–x)Cr_2O_3/$x$$K_2O$ NPs, where x = 0.1, 0.3, 0.5, and 0.7. Photocatalytic degradation occurred with a maximum of 35.6% after irradiation time of 120 min at x = 0.7. The photocatalytic process [23] is explained as a photoinduced molecular transformation occurring at the surface of the metal oxide NPs. As shown in Fig. 8, the electron–hole pair is generated when light is utilized in the photocatalytic process. When the catalyst is exposed to UV light with higher energy than its band gap, the electron is transported to the conduction band, creating a hole in the valence band. These holes are important for photocatalysis because they are a source of oxidized hydroxyl radicals that react to the electrons in the dyes [17,24].

The following equations describe the previous procedures [25]:

$$\text{catalyst}\left(\frac{Cr_2O_3}{K_2O}\right) + h\nu \rightarrow e^- + h^+ \tag{6}$$

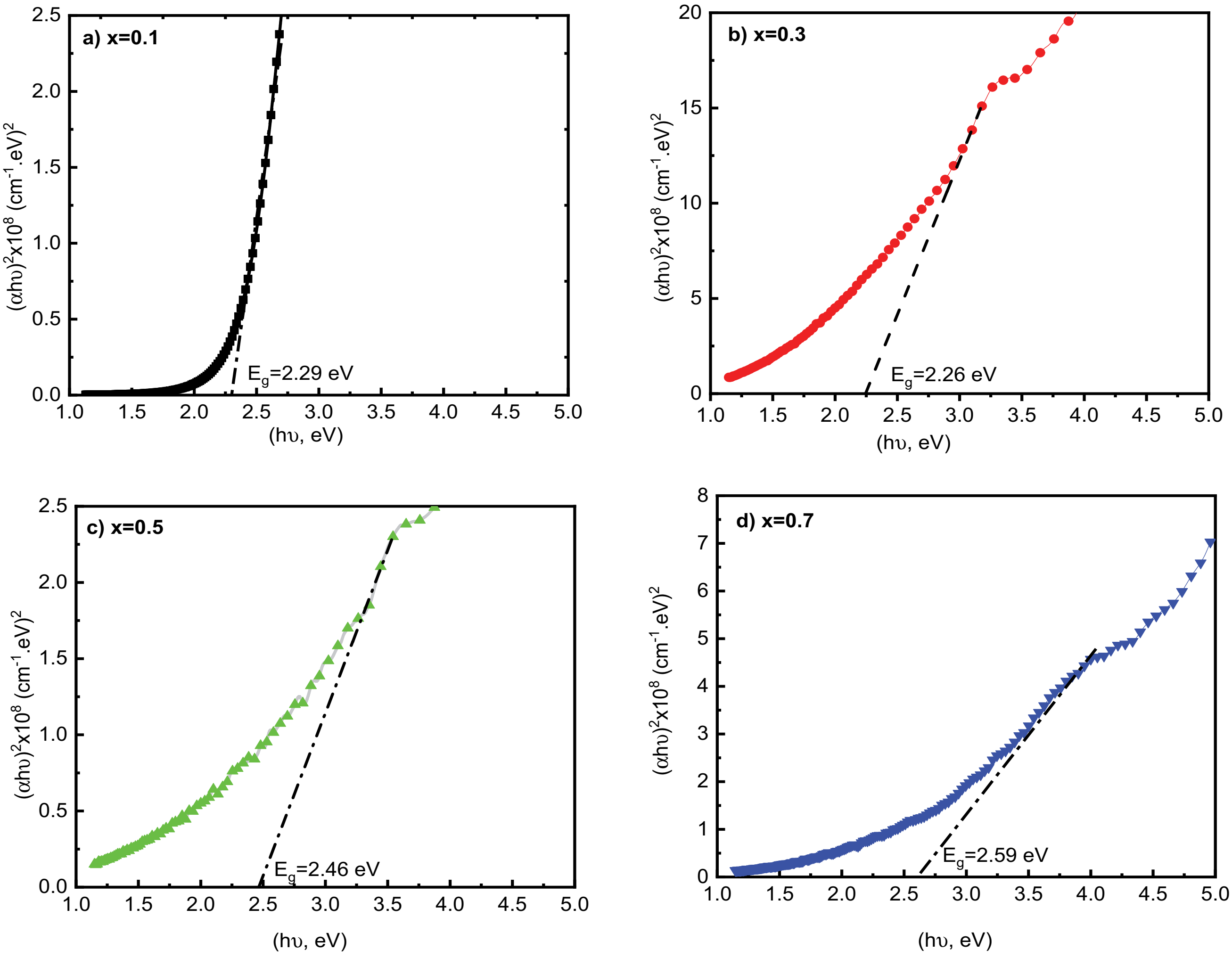

Fig. 5. Plot of $(\alpha h\upsilon)^2$ vs. photon energy ($h\upsilon$) for different concentration of (1–x)Cr_2O_3/$x$$K_2O$ NPs where (x = 0.1, 0.3, 0.5, 0.7).

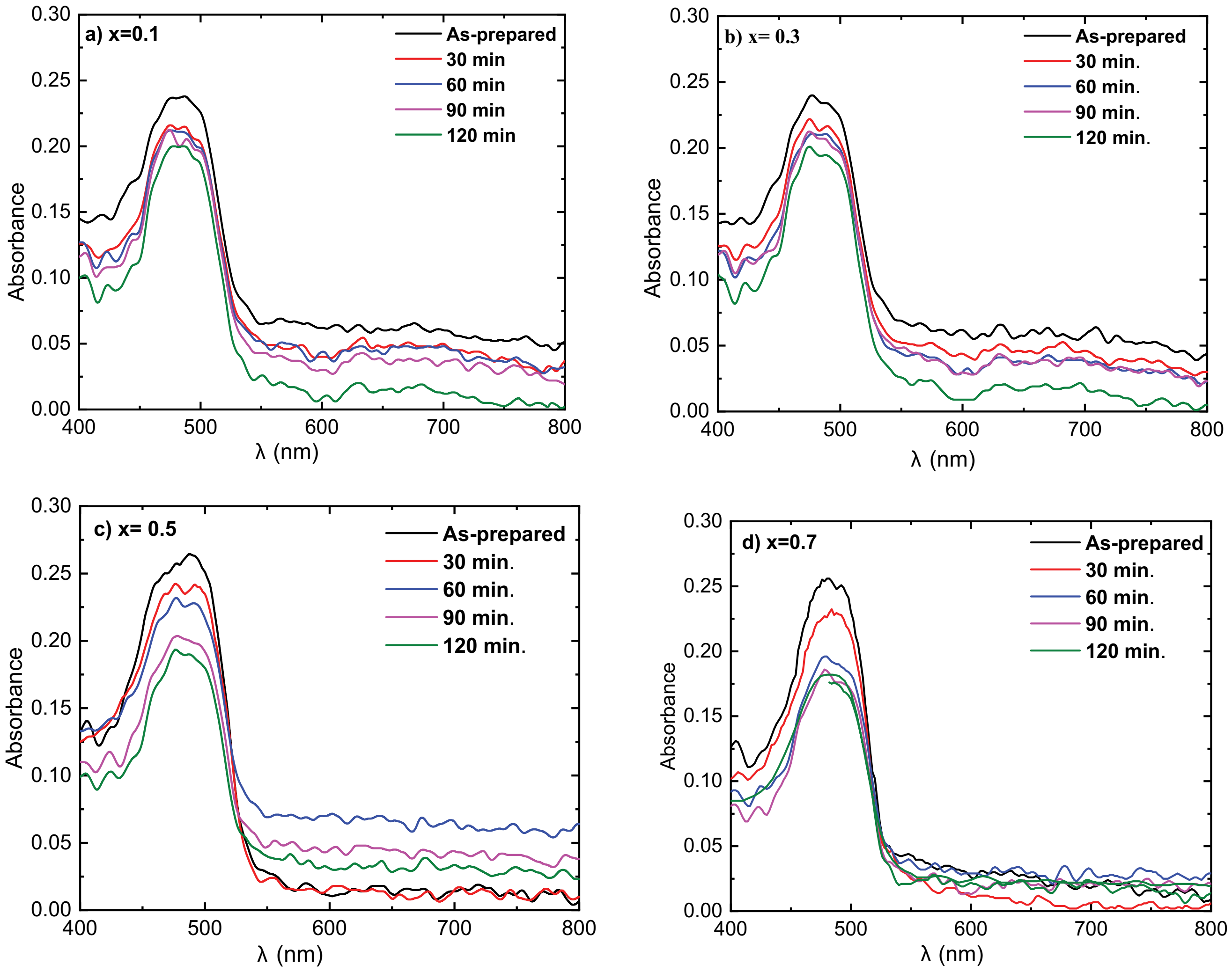

Fig. 6. Absorbance time dependence of Orange G with (1–x)Cr_2O_3/$x$$K_2O$, (a) $x = 0.1$, (b) $x = 0.3$, (c) $x = 0.5$, and (d) $x = 0.7$ as catalyst.

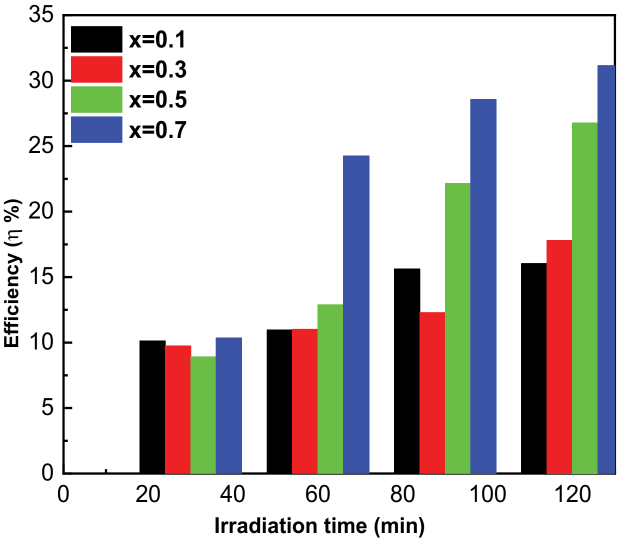

Fig. 7. The photocatalytic efficiency (η%) of Orange G debasement using (1–x)Cr_2O_3/$x$$K_2O$ (x = 0.1, 0.3, 0.5, 0.7) NPs.

$$e^- + O_2 \rightarrow O_2^- \quad (7)$$

$$h^+ + \text{Orange G} \rightarrow \text{degradation product} \quad (8)$$

$$h^+ + H_2O \rightarrow OH^- + H^+ \quad (9)$$

$$OH^- + \text{Orange G} \rightarrow \text{degradation product} \quad (10)$$

The ln(C/C_o) as a function of the irradiation time, t, is calculated by [25]:

$$\ln\left(\frac{C_t}{C_i}\right) = -kKt + KC_i \quad (11)$$

where C_i, C_t are the primary dye concentration and the rest concentration after irradiation light, t. k is the first-order reaction rate constant, and K is the degradation equilibrium at light constant. Fig. 9 illustrates the straight line produced by Eq. (11), which describes the semi-logarithmic relationship

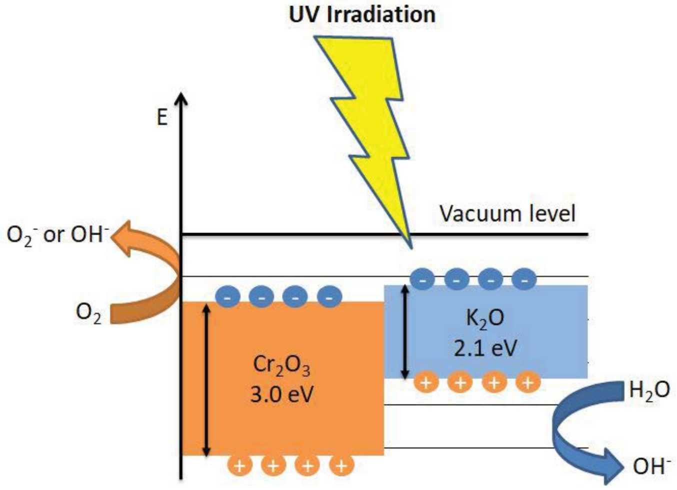

Fig. 8. Schematic illustration indicating the photocatalysis mechanism of the Cr_2O_3/xK_2O photocatalyst (The diagram is not to scale and not fully labelled).

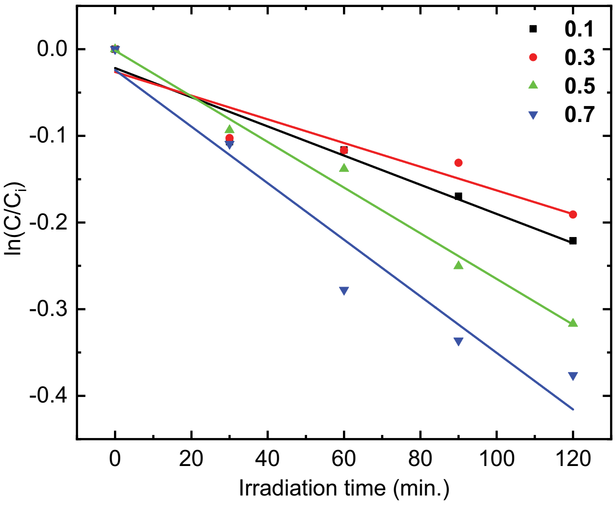

Fig. 9. Semi-logarithmic graph of Orange G concentration vs. irradiation time in the presence of $(1–x)Cr_2O_3/xK_2O$ (x = 0.1, 0.3, 0.5, 0.7) NPs.

between the Orange G concentrations as a function of the irradiation time. This formula can be used to compute the degradation equilibrium constant (K) and the degradation rate constant (k) [25] which is listed in Table 2. The determined values of the k and K constants are shown in Table 3. For Orange G, it was discovered that these k and K constants were reliant on UV light exposure as well as K_2O content.

The mass of Orange G degraded per unit of $(1–x)Cr_2O_3/xK_2O$ NPs (q, mg/g) at a fixed time and equilibrium state were calculated using the following equations [26]:

$$q_t = \left(C_i - C_t\right)\frac{V}{W} \tag{12}$$

where q_t is the quantity of degraded Orange G at time (t) in mg/g, C_i and C_t are the initial and residual concentration of degraded Orange G at time (t), respectively. V is the volume of the solution in L, and W is the mass in g.

Table 2
The absolute values of first-order reaction rate constants (k) and degradation equilibrium constant (K), for Orange G dye of $(1–x)Cr_2O_3/xK_2O$ nanoparticles

x	k	K
0.1	0.39	0.00109
0.3	0.26	0.00131
0.5	8.35	0.00008
0.7	0.68	0.00120

The relationship of degraded Orange G, q_t vs. irradiation time for $(1–x)Cr_2O_3/xK_2O$ NPs, where x = 0.1, 0.3, 0.5, and 0.7, is shown in Fig. 10. These curves show that as the irradiation time increases, the q_t values increase for all compositions of $(1–x)Cr_2O_3/xK_2O$ NPs. The impact of K_2O NPs content increases the Orange G capacity, confirming the photocatalytic procedure [27]. It can be seen that Orange G debasement has occurred in a single step. These results are comparable with previous data [20,23]. In Table 3, the results of the variation in degradation efficiency for Orange G dye are compared and summarized using different catalysis. Using pure Bi_2MoO_6 catalysts, the ultimate breakdown of Orange G dye in 300 min was 98% [28] compared with 37.16% for TiO_2-ZnO after 120 min; more results are listed in Table 3 [28–31]. Our samples give 33% of degradation efficiency after 120 min.

4. Conclusions

Different compositions of $(1–x)Cr_2O_3/xK_2O$ composites, where x = 0.1, 0.3, 0.5, and 0.7 wt.%, were synthesized using the microwave irradiation method. The structural parameters, optical band gap, E_g, and their photocatalytic degradation of Orange G were investigated. From the XRD data, the samples are crystalline and have monoclinic structures

Table 3
Comparison of catalytic efficiency of Cr_2O_3/K_2O with previous literatures

Sample	Orange G dye concentrations (mg/L)	Catalyst degradation efficiency (%)	Degradation time (min)	References
Bi_2MoO_6	(20–100)	98	300	[28]
ZnO/activated carbon	(20)	95	350	[29]
ZnO/HS	(50)	49.7	300	[30]
TiO_2-ZnO	(20)	37.2	120	[31]
	(20)	33	120	Present study

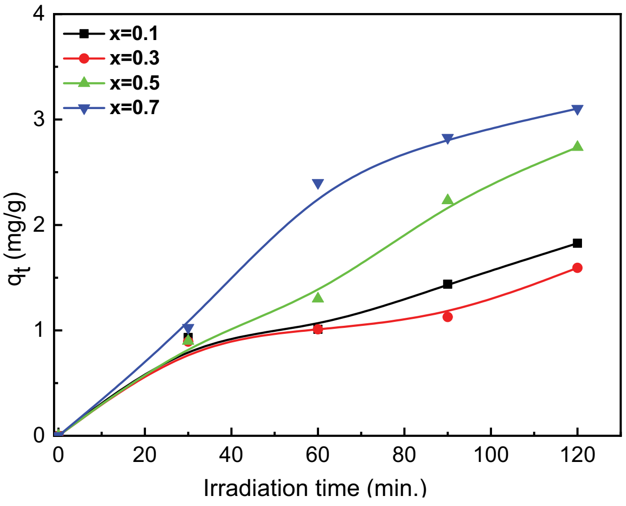

Fig. 10. Degradation capacity (q_t) of Orange G vs. illumination time on the $(1-x)Cr_2O_3/xK_2O$ (x = 0.1, 0.3, 0.5, 0.7) NPs.

of Cr_2O_3 and hexagonal structures of K_2O. The concentration of the composite components has a significant influence on the crystallite size; for example, the smaller average crystallite sizes were formed when the ratio of K_2O is 0.7 wt.%. The optical band gap of the composites was affected by their composition as it varies from 2.29 to 2.59 eV and obeys the direct allowed transition. Photocatalytic efficiency of Orange G in wastewater were investigated using $(1-x)Cr_2O_3/xK_2O$ NPs, where x = 0.1, 0.3, 0.5, and 0.7. The efficiency obtained with $(1-x)Cr_2O_3/xK_2O$, where x = 0.1 and 0.7, was 11% and 33%, respectively. The prepared $(1-x)Cr_2O_3/xK_2O$ composites could qualify for the degradation of some organic dyes for water purification assisted by UV irradiation.

References

[1] A. Fujishima, T. Rao, D. Tryk, P-doped titania xerogels as efficient UV-visible photocatalysts, J. Photochem. Photobiol., C, 1 (2000) 1–21.
[2] J. Trawiński, R. Skibiński, Multivariate comparison of photocatalytic properties of thirteen nanostructured metal oxides for water purification, J. Environ. Sci. Health. Part A Toxic/Hazard. Subst. Environ. Eng., 54 (2019) 851–864.
[3] D. Panchal, A. Sharma, S. Pal, Chapter 1 – Novel Photocatalytic Techniques for Organic Dye Degradation in Water, M. Shah, S. Dave, J. Das, Eds., Photocatalytic Degradation of Dyes: Current Trends and Future Perspectives, Elsevier, Germany, 2021, pp. 1–22.
[4] A. Dahiya, B.K. Patel, Chapter 3 – Photocatalytic Degradation of Organic Dyes Using Heterogeneous Catalysts, M. Shah, S. Dave, J. Das, Eds., Photocatalytic Degradation of Dyes: Current Trends and Future Perspectives, Elsevier, Germany, 2021, pp. 43–90.
[5] J. Singh, V. Verma, R. Kumar, R. Kumar, Influence of Mg^{2+}-substitution on the optical band gap energy of $Cr_{2-x}Mg_xO_3$ nanoparticles, Results Phys., 13 (2019) 102106, doi: 10.1016/j.rinp.2019.02.042.
[6] A.A. Salaeva, M.A. Salaev, O.V. Vodyankina, G.V. Mamontov, Synergistic effect of Cu and Zn modifiers on the activity of CrO_x/Al_2O_3 catalysts in isobutane dehydrogenation, Appl. Catal., A, 581 (2019) 82–90.
[7] G.A. El-Shobaky, A.I. Ahmed, H.M.A. Hassan, S.E. El-Shafey, Effects of K_2O–Li_2O doping on surface and catalytic properties of Fe_2O_3/Cr_2O_3 system, J. Alloys Compd., 509 (2011) 1314–1321.
[8] B.Y. Jibril, Propane oxidative dehydrogenation over chromium oxide-based catalysts, Appl. Catal., A, 264 (2004) 193–202.
[9] B.-Y. Song, X.-F. Zhang, J. Huang, X.-L. Cheng, Z.-P. Deng, Y.-M. Xu, L.-H. Huo, S. Gao, Porous Cr_2O_3 architecture assembled by nano-sized cylinders/ellipsoids for enhanced sensing to trace H_2S gas, ACS Appl. Mater. Interfaces, 14 (2022) 22302–22312.
[10] C.L. Li, H.X. Zhao, T. Takahashi, M. Matsumur, Improvement of corrosion resistance of materials coated with a Cr_2O_3/NiCr dilayer using a sealing treatment, Mater. Sci. Eng., A, 308 (2001) 268–276.
[11] V.S. Jaswal, A.K. Arora, J. Singh, M. Kinger, V.D. Gupta, Synthesis and characterization of chromium oxide nanoparticles, Orient. J. Chem. An Int. Res. J. Pure Appl. Chem., 30 (2014) 559–566.
[12] E.R. Shaaban, M.Y. Hassaan, M.G. Moustafa, A. Qasem, G.A.M. Ali, E.S. Yousef, Investigation of structural and optical properties of amorphous-crystalline phase transition of $As_{40}S_{45}Se_{15}$ thin films, Acta Phys. Pol. A, 136 (2019) 498–512.
[13] M.S. Muthu, P. Ajith, J. Agnes, R. Ramkumar, P. Raja, D. Prem Anand, Synthesis, characterizations and antibacterial studies of chromium trioxide nanoparticles, Int. J. Mod. Trends Sci. Technol., 8 (2022) 252–258.
[14] R. Viswanatha, T.G. Venkatesh, C.C. Vidyasagar, Y. Arthoba Nayaka, Y.J. Arch. Preparation and characterization of ZnO and Mg-ZnO nanoparticle, Arch. Appl. Sci. Res., 4 (2012) 480–486.
[15] M. Rashad, M. Rüsing, G. Berth, K. Lischka, A. Pawlis, CuO and Co_3O_4 nanoparticles: synthesis, characterizations, and Raman spectroscopy, J. Nanomater., 2013 (2013) 82, doi: 10.1155/2013/714853.
[16] N.M. Shaalan, M. Rashad, M.A. Abdel-Rahim, Repeatability of indium oxide gas sensors for detecting methane at low temperature, Mater. Sci. Semicond. Process., 56 (2016) 260–264.
[17] M. Rashad, N.M. Shaalan, A.M. Abd-Elnaiem, Degradation enhancement of methylene blue on ZnO nanocombs synthesized by thermal evaporation technique, Desal. Water Treat., 57 (2016) 26267–26273.
[18] N.M. Shaalan, D. Hamad, A. Aljaafari, A.Y. Abdel-Latief, M.A. Abdel-Rahim,. Preparation and characterization of developed $Cu_xSn_{1-x}O_2$ nanocomposite and its promising methane gas sensing properties, Sensors, 19 (2019) 2257, doi: doi: 10.3390/s19102257.

[19] R.A. Zargar, K. Kumar, Z.M.M. Mahmoud, M. Shkir, S. AlFaify, Optical characteristics of ZnO films under different thickness: a MATLAB-based computer calculation for photovoltaic applications, Physica B, 631 (2022) 413614, doi: 10.1016/j.physb.2021.413614.

[20] H.A. Al-Aoh, M. Jamil Maah, R. Yahya, M. Radzi Bin Abas, A comparative investigation on adsorption performances of activated carbon prepared from coconut husk fiber and commercial activated carbon for Acid Red 27 dye, Asian J. Chem., 25 (2013) 9582–9590.

[21] H. Zhu, R. Jiang, Y. Fu, Y. Guan, J. Yao, L. Xiao, G. Zeng, Effective photocatalytic decolorization of methyl orange utilizing TiO_2/ZnO/chitosan nanocomposite films under simulated solar irradiation, Desalination, 286 (2012) 41–48.

[22] P. Zhang, X. Sun, J. Guo, Y. Wang, W. Zhang, W. Ning, W. Li, C. Wei, X. Shi, S. Miao, Deep-sea clays using as active Fenton catalysts for self-propelled motors, J. Am. Ceram. Soc., 105 (2022) 3797–3808.

[23] M. Rashad, T.A. Hamdalla, A.A.A. Darwish, S.M. Seleim, High performance efficiency of water purification using Cr_2O_3 nanoparticles synthesized by thermal combustion technique, Mater. Res. Express, 6 (2019) 065048.

[24] M.L. Curri, R. Comparelli, P.D. Cozzoli, G. Mascolo, A. Agostiano, Colloidal oxide nanoparticles for the photocatalytic degradation of organic dye, Mater. Sci. Eng., C, 23 (2003) 285–289.

[25] N.M. Shaalan, M. Rashad, O. Saber, A. Alshoaibi, C. Awada, A comprehensive photocatalysis study of promising zirconia/laser-induced graphene nanocomposite for wastewater treatment-based methylene blue pollution, Separations, 9 (2022) 185, doi: 10.3390/separations9080185.

[26] A. Fisal, W.M.A.W. Daud, M.A. Ahmad, R. Radzi, Using cocoa (*Theobroma cacao*) shell-based activated carbon to remove 4-nitrophenol from aqueous solution: kinetics and equilibrium studies, Chem. Eng. J., 178 (2011) 461–467.

[27] A.A.A. Darwish, M. Rashad, H.A. AL-Aoh, Methyl orange adsorption comparison on nanoparticles: isotherm, kinetics, and thermodynamic studies, Dyes Pigm., 160 (2019) 563–571.

[28] B.K. Shukla, S. Rawat, M.K. Gautam, H. Bhandari, S. Garg, J. Singh, Photocatalytic degradation of Orange G dye by using bismuth molybdate: photocatalysis optimization and modeling via definitive screening designs, Molecules, 27 (2022) 2309, doi: 10.3390/molecules27072309.

[29] M. Vinayagam, R. Saranya, V. Ramya, A. Sivasamy, Photocatalytic degradation of Orange G dye using ZnO/biomass activated carbon nanocomposite, J. Environ. Chem. Eng., 6 (2017) 3726–3734.

[30] A.A. Al-Beladi, S.A. Kosaa, R.A. Wahab, M.A. Salam, Removal of Orange G dye from water using halloysite nanoclay-supported ZnO nanoparticles, Desal. Water Treat., 196 (2020) 287–298.

[31] M.A.B. Samad, M.A. Hossain, T.S.A. Islam, W. Farha, Photodegradation of Orange G as an environmental pollutant with TiO_2-ZnO composite material, Fine Chem. Eng., 3 (2021) 29–38.